
Article:
Yang, B., Xu, H., Liu, W. orcid.org/0000-0003-2968-2888 et al. (2 more authors) (2018) A novel statistical model for differential synthetic aperture radar tomography. Measurement Science and Technology, 29 (9). 095404. ISSN 0957-0233

https://doi.org/10.1088/1361-6501/aad3a9

A Novel Statistical Model for Differential SAR Tomography

Bo Yang[1], Huaping Xu[1], Wei Liu[2], Yao Luo[1] and Shouyou Huang[3]

[1] School of Electronic and Information Engineering, Beihang University, Beijing, China

[2] Department of Electronic and Electrical Engineering, University of Sheffield, S1 4ET, Sheffield, U.K.

[2] School of Mathematics and statistics, Hubei Normal University, Huangshi, China

E-mail: xuhuaping@buaa.edu.cn (corresponding author)

April 2018

Abstract. Deterministic differential Tomographic SAR (D-TomoSAR) model, based on geometrical derivations and the assumption of accurate phase calibration, is widely employed for spatially locating and temporally monitoring the point-like scatterers in the past. In this work, we model phase miscalibration effects of the extended scatters caused by partial correlation, i.e., the decorrelation effects from temporal and spatial changes as well as the residual atmospheric and deformation effect after preprocessing. Starting from the origin of 4-D SAR focusing, correlation of target is analysed, and a statistical D-TomoSAR model accounting for partial correlation effects is proposed. Based on the proposed model, a simulator for D-TomoSAR stack is designed using the Cholesky decomposition. Moreover, a linear minimum mean square error (LMMSE) estimator based on the proposed model is developed for height and deformation velocity estimation of extended scatterer. Reconstruction results with both simulated data and real data acquired by TerraSAR-X/Tandem-X sensors are provided to demonstrate the effectiveness of the proposed model.

1. Introduction

Nowadays, many high resolution synthetic aperture radar (SAR) sensors are available in orbits, such as the COSMO-SKYMED constellation with a high revisit frequency and TerraSAR-X/Tandem-X (a pair of cooperating satellites) capable of acquiring interferometric data simultaneously on a single orbit. As a result, development of multi-image SAR coherent combination techniques is of great interest to improve the estimation performance for various target properties.

Tomographic sythetic aperture radar (TomoSAR) is a technique based on coherent SAR data combination for 3-D SAR imaging [1–5]. Multi-pass acquisitions or simultaneous acquisitions with slight difference in perspective are stacked to synthesize an array along the elevation direction. The TomoSAR technique allows one to profile

the scattering power at different heights, and hence can not only locate a single scatterer more accurately but also separate the interfering scatterers within the same azimuth-range pixel more effectively [6–8]. However, it does not take into account the movements of possible scatterers. For this reason, differential SAR tomography (D-TomoSAR) or 4-D SAR imaging have been proposed to jointly estimate multiple scatterer elevations and velocities [9, 10].

The state-of-the-art D-TomoSAR signal model is deterministic with the assumption of accurate phase calibration, that is, absence of residual effect after preprocessing of D-TomoSAR [6, 7, 11]. However, on one hand, the acquisition rate associated with current systems is fixed on a monthly basis, and hence, the collection of data useful for 4-D imaging commonly requires temporal spans at the order of years. On the other hand, spatial difference in look angle will also lead to variation of the scatterer response. Thus, the coherence of targets is reduced [12]. Therefore, the decorrelation effects from temporal and spatial diversity can result in changes of focusing scattering between multiple acquisitions. As a result, only the reflectivity of point-like scatterers, whose phases are stable, could be estimated effectively with the deterministic model [8, 13]. Thus, the capability of D-TomoSAR is limited to urban areas and man-made objects where there are many point-like scatterers [8].

To expand the 4D deterministic model's application, several methods are developed to alleviate the decorrelation effects. For example, the small baseline subsets are adopted to reduce the spatial decorrelation effect [14, 15], at the cost of a low elevation and deformation resolution, or some kind of coherent averaging is performed over different sub-images of the same scene, which unfortunately results in an azimuth-range resolution loss [16]. However, there are still some uncompensated phase and random phase noise resulting from the spatial and temporal decorrelation. Therefore, the deterministic model is not realistic for the 4D SAR focusing.

Subsequently, some statistical models are presented to model the residual effects. Ignoring deformation of scatterers, a statistical TomoSAR model accounting for decorrelation effects of extended scatterers was studied by Gini et al. [16]. However, the model is not applicable to the point-like scatters and at the cost of spatial resolution due to the employment of multilook estimators. After the temporal decorrelation model proposed by Rocca [17], Fornaro et al. [11] introduced a set of parameters accounting for the residual atmospheric effect and the temporal effect of target reflectivity into the deterministic TomoSAR model, and then applied the linear minimum mean square error (LMMSE) estimator to the model, which ignores the spatial decorrelation effect. Subsequently, Pauciullo et al. [18] proposed the concept of coherence space for scatterer detection of 3-D SAR, while ignoring the residual disturbance from atmospheric delay in order to derive the analytical expression of the detector.

Taking the drawbacks of statistical TomoSAR models and deformation into consideration, we propose a statistical D-TomoSAR model in which the spatial and temporal decorrelation and residual effect after preprocessing of the extended and point-like scatterers are simultaneously accounted for. In detail, starting from the origin of 4-D

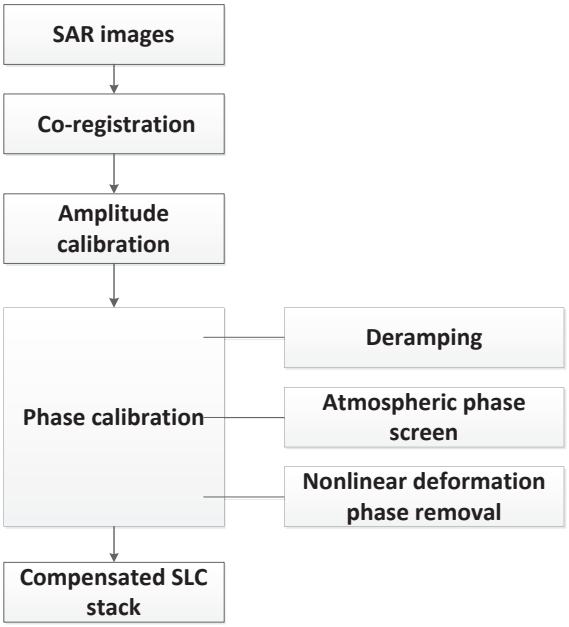

Figure 1. The preprocessing flowchart of D-TomoSAR technique.

SAR focusing, correlation of targets is analysed and the disturbances are introduced, and then reasonable distributions are assumed to model the disturbances based on the mathematical approximation and on the condition of satisfying the correlation expressions. After that, a simulator for generating the repeated pass data with realistic effects is designed based on the proposed model. With the study of statistical characteristics of the signal model, the LMMSE estimator is designed to estimate the elevations and mean deformation velocities of general scatterers. Simulation results on simple pixels and complex scene are provided to demonstrate the effectiveness of the proposed model.

2. Deterministic D-TomoSAR model

The conventional D-TomoSAR model does not consider deterministic phase miscalibration after preprocessing (the preprocessing flowchart showing in Fig. 1 [6, 19]) and random scattering changes due to the temporal and spatial decorrelation effects [20]. Thus, after preprocessing, a generic pixel of the k-th high-resolution SAR image can be modeled by the following double line integration [1, 8, 9, 21–23]

$$y_k = \int_{S_{\min}}^{S_{\max}} \int_{V_{\min}}^{V_{\max}} \gamma(s,v) \exp(j2\pi\xi_k s + j2\pi\eta_k v) ds dv + w_k \tag{1}$$

where $[S_{min}, S_{max}]$ and $[V_{min}, V_{max}]$ are the elevation and velocity span along the direction s and v respectively, $j = \sqrt{-1}$, w_k is the additive noise including the effects of clutters and thermal noise, $\gamma(s, v)$ is the complex target backscattering at the elevation position s and the velocity position v, $\xi_k = 2b_{\perp k}/\lambda r$ and $\eta_k = 2t_k/\lambda$ are the spatial

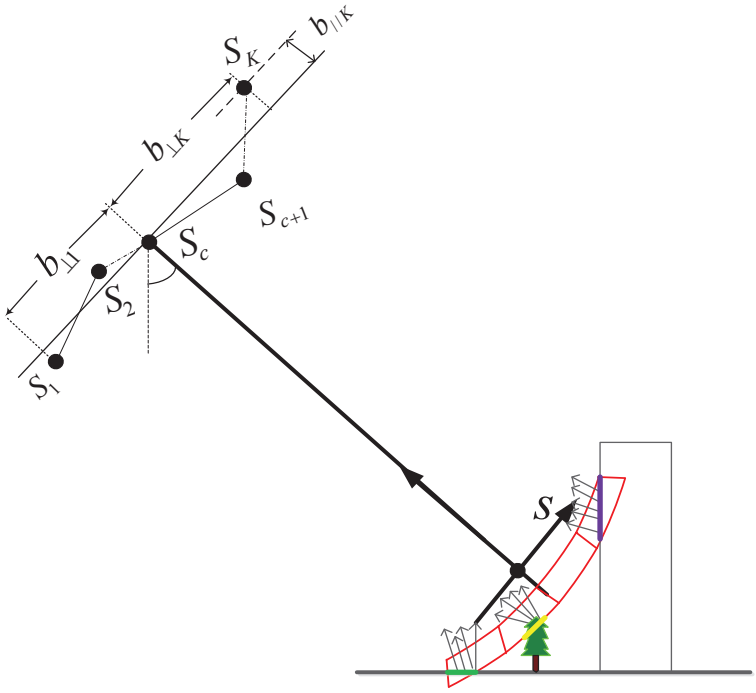

Figure 2. D-TomoSAR acquisition geometry.

and temporal frequency, respectively, λ and r are radar wavelength and the local range respectively, $b_{\perp k}$ is the effective baseline vertical to the range direction of the master antenna S_c as shown in Fig. 2, and t_k is the observing time of the k-th SAR image. Temporal and spatial baselines are defined with respect to a reference master antenna. Fig. 2 shows the D-TomoSAR acquisition geometry in the range-elevation plane orthogonal to the azimuth direction, where K views are collected at different acquisition times. After uniform partition along the elevation direction as shown by the red sector areas of Fig. 2, the pixel value of the k-th observation y_k can be written as a linear combination in its discrete form,

$$y_k = \sum_{m=1}^{M} \sum_{n=1}^{N} \mathbf{\Phi}(k, m, n) x_{mn} + w_k \tag{2}$$

where $\mathbf{\Phi}(k, m, n) = \exp(j2\pi\xi_k s_m + j2\pi\eta_k v_n)$ for $k = 1, 2, \cdots, K$, $m = 1, 2, \cdots, M$ and $n = 1, 2, \cdots, N$, s_m and v_n are the elevation and velocity of target, respectively, and x_{mn} is complex focusing of targets.

Subsequently, the K sets of differential tomographic SAR data can be modeled linearly

$$\mathbf{y} = \sum_{m=1}^{M} \sum_{n=1}^{N} \mathbf{\Phi}(s_m, v_n) x_{mn} + \mathbf{w} \tag{3}$$

where $\mathbf{y}$ with the size of $K \times 1$ is the joint observations at the referred azimuth-range cell, and $\mathbf{\Phi}(s_m, v_n)$ is the steering vector at the elevation s_m and velocity v_n. Since the clutter samples are weakly correlated, the cluttering effect can be embedded into the

additive white noise contribution, and thus $\mathbf{w}$ is assumed to be zero-mean Gaussian with a covariance matrix $\sigma_{\mathrm{w}}^2\mathbf{I}$, where σ_{w}^2 is the intensity of additive noise and $\mathbf{I}$ is the $K \times K$ identity matrix.

3. Statistical D-TomoSAR model

With the current technology, the multi-baseline data are usually acquired on repeated passes. Although the complex reflectivity of a target is strongly correlated among different observations, they still suffer the multiplicative noise effects resulting from three factors [11, 18, 20, 24, 25]:

• Temporal decorrelation of target reflectivity: change of vegetation cover and topographic changes.

• Spatial decorrelation of target reflectivity: incident angle difference because of the spatial baseline of multi-passes.

• Residual phase effect after preprocessing: the residual phase which is not compensated completely at the preprocessing stage.

3.1. Correlation analysis of target

After the preprocessing of D-TomoSAR, the phase left for the m-th scatterer should be $(j2\pi\xi_k s_m + j2\pi\eta_k v_m)$ in the ideal case. However, there exists residual phase θ_k resulting from uncompensated atmospheric delay and nonlinear deformation. The residual phases between different acquisitions are usually assumed to be zero-mean, independent and identically distributed (i.i.d.) with variance σ_θ^2 [26]. When $[S_{min},\, S_{max}]$ and $[V_{min},\, V_{max}]$ in Eq. (1) are discretized with M and N uniform segments, the focusing of 4-D scattering contributed by the patch (s_m, v_n) at the time of t_k can be written by

$$x_k\left(s_m, v_n\right) = \int_{s_m-\frac{\rho_s}{2}}^{s_m+\frac{\rho_s}{2}} \int_{v_n-\frac{\rho_v}{2}}^{v_n-\frac{\rho_v}{2}} \gamma\left(s, v\right) e^{j2\pi\xi_k(s-s_m)+j2\pi\eta_k(v-v_n)+j\theta_k} ds dv, \quad (4)$$

where $\gamma\left(s, v\right)$ denotes the backscattering profile at elevation s and velocity v, ρ_s and ρ_v are the discrete elevation and velocity interval of respective span.

When the backscattering profile $\gamma(s, v)$ in Eq. (4) is assumed to be a white complex random process in elevation and deformation velocity direction, the correlation of backscattering profile is assumed as

$$E\left[\gamma\left(s_1, v_1\right)\gamma(s_2, v_2)^*\right] = \frac{\sigma_x^2}{\rho_s\rho_v}\delta(s_1 - s_2)\delta(v_1 - v_2) \quad (5)$$

where σ_x^2 denotes the mean intensity of patches with an area of $\rho_s \times \rho_v$ and $\delta(\cdot)$ is the continuous delta function. It is worth noting that $\hat{\delta}(\cdot)$ represents the discrete delta function in this paper.

On the basis of Eq. (5), the correlation function of 4-D focusing can be written as (detail derivation is shown in Appendix A)

$$\begin{aligned} E\left[x_{k_1}\left(s_{m_1}, v_{n_1}\right) x_{k_2}(s_{m_2}, v_{n_2})^*\right] = \sigma_x^2(\mu_a^2)^{1-\hat{\delta}(k_1-k_2)}\hat{\delta}(s_{m_1} - s_{m_2}) \\ \cdot\hat{\delta}(v_{n_1} - v_{n_2}) sinc(\tfrac{2\rho_s \triangle \mathbf{b}_{k_1k_2}}{\lambda r}) sinc(\tfrac{2\rho_v \triangle \mathbf{t}_{k_1k_2}}{\lambda}) \end{aligned} \quad (6)$$

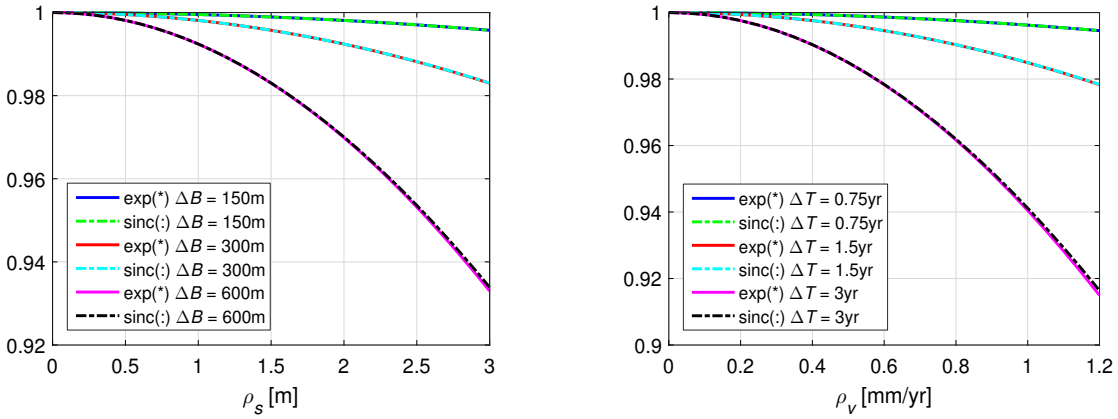

(a) (b)

Figure 3. The equivalence analysis under the Tomo-SAR parameters of the TerraSAR system. (a) $sinc(\frac{2\rho_s \Delta B}{\lambda r})$ and $\exp(-\frac{2\pi^2\rho_s^2|\Delta B|^2}{3\lambda^2 r^2})$, (b) $sinc(\frac{2\rho_v \Delta T}{\lambda})$ and $\exp(-\frac{2\pi^2\rho_v^2|\Delta T|^2}{3\lambda^2})$. Parameters: off-nadir angle $\xi = 23^o$, height of satellite $H = 520$Km, height of target $h = 0$m, $\lambda = 0.03125$m.

where $\triangle \mathbf{b}_{k_1k_2} = b_{\perp k_1} - b_{\perp k_2}$, $\triangle \mathbf{t}_{k_1k_2} = t_{k_1} - t_{k_2}$, $\mu_a = \exp(-\sigma_\theta^2)$. The terms $sinc(\cdot)$ introduced in Eq. (6) represent the spatial decorrelation and temporal decorrelation, and $(\mu_a^2)^{1-\hat{\delta}(k_1-k_2)}$ represents the residual effects. Since $sinc(x) \approx 1 - \frac{\pi^2 x^2}{6} \approx \exp(-\frac{\pi^2 x^2}{6})$ for $x \to 0$, under the condition of small interval ρ_s and ρ_v, $sinc(\frac{2\rho_s \triangle \mathbf{b}_{k_1k_2}}{\lambda r})$ and $sinc(\frac{2\rho_v \triangle \mathbf{t}_{k_1k_2}}{\lambda})$ are approximately equal to $\exp(-\frac{2\pi^2\rho_s^2 \left|\triangle \mathbf{b}_{k_1k_2}\right|^2}{3\lambda^2 r^2})$ and $\exp(-\frac{2\pi^2\rho_v^2 \left|\triangle \mathbf{t}_{k_1k_2}\right|^2}{3\lambda^2})$, respectively, as shown in Fig. 3. Thus, Eq. (6) can be transferred to

$$\begin{aligned} E\left[x_{k_1}(s_{m_1}, v_{n_1})\, x_{k_2}(s_{m_2}, v_{n_2})^*\right] \approx \sigma_x^2 (\mu_a^2)^{1-\hat{\delta}(k_1-k_2)} \cdot \hat{\delta}(s_{m_1} - s_{m_2}) \\ \cdot \hat{\delta}(v_{n_1} - v_{n_2}) \exp(-\frac{2\pi^2\rho_s^2 \left|\triangle \mathbf{b}_{k_1k_2}\right|^2}{3\lambda^2 r^2} - \frac{2\pi^2\rho_v^2 \left|\triangle \mathbf{t}_{k_1k_2}\right|^2}{3\lambda^2}) \end{aligned} \tag{7}$$

Based on the above analysis, we use the multiplicative factor $a_k = \exp(-j\theta_k)$ to represent the residual phase effects, and introduce another two multiplicative factors for 4-D scattering to account for the exponential term in Eq. (7). Mathematically, $d_k(s_m) = \exp(-j\nu_k(s_m))$ and $\tau_k(v_n) = \exp(-j\vartheta_k(v_n))$ resulting from spatial and temporal decorrelation respectively are introduced to separate the scattering target x_{mn} from the decorrelated target $x_k(s_m, v_n)$

$$x_k(s_m, v_n) = a_k d_k(s_m) \tau_k(v_n) x_{mn} \tag{8}$$

According to Eq. (7), the correlation function of a_{k_1} and a_{k_2} is $(\mu_a^2)^{1-\hat{\delta}(k_1-k_2)}$, the correlation function of $d_{k_1}(s_m)$ and $d_{k_2}(s_m)$ is $\exp(-\frac{2\pi^2\rho_s^2 \left|\triangle \mathbf{b}_{k_1k_2}\right|^2}{3\lambda^2 r^2})$, and that of $\tau_{k_1}(v_n)$ and $\tau_{k_2}(v_n)$ is $\exp(-\frac{2\pi^2\rho_v^2 \left|\triangle \mathbf{t}_{k_1k_2}\right|^2}{3\lambda^2})$. The common assumption that the temporal decorrelation is of exponential decay [11, 17, 18, 27], is similar to ours, except that the time constant of the coherence decay should be given firstly.

3.2. Statistical model

Introducing the multiplicative factors of Eq. (8) into Eq. (2), each pixel of the resulting SAR image can be generally expressed as

$$y_k = \sum_{m=1}^{M}\sum_{n=1}^{N} a_k d_k(s_m)\tau_k(v_n)\mathbf{\Phi}(k,m,n)x_{mn} + w_k. \tag{9}$$

As a consequence, for each pixel, the signal model with the K considered acquisitions can be written as

$$\mathbf{y} = \sum_{m=1}^{M}\sum_{n=1}^{N} \mathbf{a}\odot\mathbf{d}_m\odot\boldsymbol{\tau}_n\odot\mathbf{\Phi}(s_m,v_n)x_{mn} + \mathbf{w} \tag{10}$$

where $\odot$ is the Hadamard product, and the vectors of multiplicative noise $\mathbf{a} = \exp(-j\boldsymbol{\theta})$, $\mathbf{d}_m = \exp(-j\boldsymbol{\nu}_m)$ and $\boldsymbol{\tau}_n = \exp(-j\boldsymbol{\vartheta}_n)$ are extensions from the case with one pair of images. Then, their corresponding correlation matrices can be expressed as

$$\begin{aligned}
\mathbf{R}_{\mathbf{a}} &= \exp(-2\sigma_\theta^2)\,\mathbf{e}\cdot\mathbf{e}^{\mathrm{T}} + [1-\exp(-2\sigma_\theta^2)]\,\mathbf{I}\\
\mathbf{R}_{\mathbf{d}} &= \exp(-\frac{2\pi^2\rho_s^2\triangle\mathbf{b}\odot\triangle\mathbf{b}}{3\lambda^2 r^2})\\
\mathbf{R}_{\boldsymbol{\tau}} &= \exp(-\frac{2\pi^2\rho_v^2\triangle\mathbf{t}\odot\triangle\mathbf{t}}{3\lambda^2})
\end{aligned} \tag{11}$$

where $\mathbf{e}$ is a vector with all one elements. When temporal and spatial decorrelations as well as residual phase resulting from atmospheric and deformation are ignored, the above statistical D-TomoSAR model (Eq. (10)) is then simplified to the deterministic one (Eq. (3)).

To derive elevation and deformation velocity estimation algorithms for the general model, the vectors of multiplicative noise should be modeled with reasonable distributions. Given the exponential expressions in Eq. (11), here $\boldsymbol{\theta}$, $\boldsymbol{\nu}_m$ and $\boldsymbol{\vartheta}_n$ are modeled by zero-mean real multivariate Gaussian distributions, with their correlation matrices given by

$$\begin{aligned}
\mathbf{R}_{\boldsymbol{\theta}} &= \sigma_\theta^2\mathbf{I}\\
\mathbf{R}_{\boldsymbol{\nu}} &= \sigma_\nu^2\mathbf{e}\cdot\mathbf{e}^{\mathrm{T}} - \frac{2\pi^2\rho_s^2\triangle\mathbf{b}\odot\triangle\mathbf{b}}{3\lambda^2 r^2}\\
\mathbf{R}_{\boldsymbol{\vartheta}} &= \sigma_\vartheta^2\mathbf{e}\cdot\mathbf{e}^{\mathrm{T}} - \frac{2\pi^2\rho_v^2\triangle\mathbf{t}\odot\triangle\mathbf{t}}{3\lambda^2}
\end{aligned} \tag{12}$$

where σ_ν^2 and σ_ϑ^2 are the variances of the elements of ν and ϑ, respectively. Here we select the minimum variance value to ensure the covariance matrix to be positive semidefinite

$$\begin{aligned}
\sigma_\nu^2 &= \frac{2\pi^2\rho_s^2\cdot\mathbf{e}^{\mathrm{T}}(\triangle\mathbf{b}\odot\triangle\mathbf{b})\mathbf{e}}{3\lambda^2 r^2}\\
\sigma_\vartheta^2 &= \frac{2\pi^2\rho_v^2\cdot\mathbf{e}^{\mathrm{T}}(\triangle\mathbf{t}\odot\triangle\mathbf{t})\mathbf{e}}{3\lambda^2}.
\end{aligned} \tag{13}$$

With the above choice of σ_ν^2 and σ_ϑ^2, the mean vectors of $\mathbf{d}_m$ and $\boldsymbol{\tau}_n$ are given by

$$\begin{aligned}
\boldsymbol{\mu}_{\mathbf{d}} &= \mu_d\mathbf{e}\\
\boldsymbol{\mu}_{\boldsymbol{\tau}} &= \mu_\tau\mathbf{e}
\end{aligned} \tag{14}$$

Table 1. $\boldsymbol{\mu}_{\mathbf{y}}, \mathbf{R}_{\mathbf{a}}, \mathbf{R}_{\mathbf{d}}$ and $\mathbf{R}_{\boldsymbol{\tau}}$ in the extreme case of $\sigma_\theta^2, \rho_s, \rho_v$.

$\sigma_\theta^2, \rho_s, \rho_v$	$\boldsymbol{\mu}_{\mathbf{y}}$	$\mathbf{R}_{\mathbf{a}}, \mathbf{R}_{\tau}, \mathbf{R}_{\mathbf{d}}$
∞	$0 \cdot \mathbf{e}$	$\mathbf{I}$
0	$\sum_{m=1}^{M} \sum_{n=1}^{N} \boldsymbol{\Phi}(k,m,n) x_{mn}$	$\mathbf{e}\mathbf{e}^{\mathrm{T}}$

where $\mu_d = \exp(-\sigma_\nu^2)$ and $\mu_\tau = \exp(-\sigma_\vartheta^2)$.

Finally, the multiplicative vectors affecting different sources are assumed to be i.i.d.. In terms of the statistical characteristics for the whole observed signal for a given stack, according to Eqs. (10), (11) and (14), the mean vector and correlation matrix are calculated by

$$\boldsymbol{\mu}_{\mathbf{y}} = \mu_a \mu_\tau \mu_d \sum_{m=1}^{M} \sum_{n=1}^{N} \boldsymbol{\Phi}(s_m, v_n) x_{mn} \tag{15}$$

$$\mathbf{R}_{\mathbf{y}} = \sum_{m=1}^{M} \sum_{n=1}^{N} \left(\mathbf{H}_{mn} x_{mn} \mathbf{R}_c x_{mn}^{\mathrm{H}} \mathbf{H}_{mn}^{\mathrm{H}} \right) + \sigma_{\mathrm{w}}^2 \mathbf{I} \tag{16}$$

where $\mathbf{H}_{mn}$ denotes the diagonal matrix obtained by diagonalizing the vector $\boldsymbol{\Phi}(s_m, v_n)$ for $m = 1, 2, \cdots, M$ and $n = 1, 2, \cdots, N$, and $\mathbf{R}_{\mathbf{c}}$ is given by

$$\mathbf{R}_{\mathbf{c}} = \mathbf{R}_{\mathbf{a}} \odot \mathbf{R}_{\boldsymbol{\tau}} \odot \mathbf{R}_{\mathbf{d}}. \tag{17}$$

In the correlation matrix expression (Eq. (16)), in addition to temporal and spatial decorrelations and residual phase effects, there also exist channel decorrelation from $\mathbf{H}_{mn}$ and additive noise decorrelation from σ_{w}^2.

As can be seen from Tab. 1, for $\rho_s \to \infty$ or $\rho_v \to \infty$ or $\sigma_\theta^2 \to \infty$, there is a fully incoherent effect affecting the target, and the mean value of signal acquired from the mn-th scatterer goes down to zero. Therefore, no useful information can be found from the observations to reconstruct the scattering distribution in the elevation-velocity plane with the given signal model. On the contrary, when $\rho_s = 0$, $\rho_v = 0$ and $\sigma_\theta^2 = 0$, the target is fully coherent with the same random disturbances for different acquisitions, and then the statistical model is simplified to the deterministic one. It's worth noting that when the intervals of different observations are short and $\rho_s = 0$, the target appears like a point, that is why the reflectivity of point-like scatterers could be estimated effectively with the deterministic model [1, 2, 6, 8]. When the proposed model of Eq. (9) is applied in the case of TomoSAR by ignoring the deformation, different from the model in [11], the spatial decorrelation effect is added and the temporal correlation matrix is derived by system parameters.

4. Data simulator and LMMSE estimator

4.1. Data simulator

Since the repeated pass data are necessary for algorithm study and system analysis of multi-baseline InSAR, a simulator to generate observed stacks is designed based on the general model in Eq. (10). In principle, $\mathbf{a}$, $\mathbf{d}_m$ and $\boldsymbol{\tau}_n$ for the mn-th scatter are generated successively from the corresponding phase vectors, which are modeled by zero-mean real multivariate Gaussian distributions with their corresponding correlation matrixes. Then, $\boldsymbol{\Phi}(s_m, v_n)$ and x_{mn} over $\mathbf{w}$ are deterministically and randomly given by the parameters of targets s_m, v_n and SNR_{mn}. Finally, the data are produced by substituting the parameters into Eq. (10).

However, due to the superposition of sparse scatterers into one pixel, the number of scatterers N_s is much less than $M \times N$. In order to simplify the generation process, we adopt the following sparse model instead of Eq. (10),

$$\mathbf{y} = \sum_{m=1}^{N_s} \exp\left(j\boldsymbol{\phi}_m\right) \odot \boldsymbol{\Phi}(s_m, v_m) x_m + \mathbf{w} \tag{18}$$

where $\boldsymbol{\phi}_m$ represents the phase vector of all multiplicative disturbances, that is, $\boldsymbol{\phi}_m = \boldsymbol{\theta} + \boldsymbol{\vartheta}_m + \boldsymbol{\nu}_m$. Thus, $\boldsymbol{\phi}_m$ is of zero-mean real multivariate Gaussian distribution, with correlation matrix $\mathbf{R}_{\boldsymbol{\phi}_m} = \mathbf{R}_{\boldsymbol{\theta}} + \mathbf{R}_{\boldsymbol{\vartheta}_m} + \mathbf{R}_{\boldsymbol{\nu}_m}$, and the generation of $\boldsymbol{\theta}$, $\boldsymbol{\vartheta}_m$ and $\boldsymbol{\nu}_m$ are reduced to the generation of $\boldsymbol{\phi}_m$. Due to the positive definite property of $\mathbf{R}_{\boldsymbol{\phi}_m}$, we decompose it using the Cholesky decomposition, that is,

$$\begin{aligned} \mathbf{R}_{\boldsymbol{\phi}_m} = E\left(\boldsymbol{\phi}_m \boldsymbol{\phi}_m^{\mathrm{H}}\right) &= E\left(\mathbf{V}\bar{\boldsymbol{\phi}}_m \bar{\boldsymbol{\phi}}_m^{\mathrm{H}} \mathbf{V}^{\mathrm{H}}\right) \\ &= \mathbf{V} E\left(\bar{\boldsymbol{\phi}}_m \bar{\boldsymbol{\phi}}_m^{\mathrm{H}}\right) \mathbf{V}^{\mathrm{H}} = \mathbf{V}\mathbf{V}^{\mathrm{H}} \end{aligned} \tag{19}$$

where $\mathbf{V}$ is the lower triangular matrix of the $\mathbf{R}_{\boldsymbol{\phi}_m}$ Cholesky decomposition, $\bar{\boldsymbol{\phi}}_m$ follows a real white Gaussian distribution with zero mean and covariance matrix $\mathbf{I}$.

Accordingly, $\boldsymbol{\phi}_m$ is generated by the product of $\mathbf{V}$ and $\bar{\boldsymbol{\phi}}_m$. Then, $\boldsymbol{\Phi}(s_m, v_m)$ and x_m over $\mathbf{w}$ are deterministically and randomly given by the parameters of targets s_m, v_m and SNR_m ($m = 1 \cdots N_s$). The data simulation flowchart of the multi-baseline InSAR is shown in Fig. 4.

4.2. LMMSE estimator

Subsequently, we design a Bayesian estimator for the unknown reflectivity $\mathbf{x} = [x_1 \cdots x_{MN}]$ in Eq. (10) based on the LMMSE approach. According to the Bayesian Gauss-Markov Theorem [28], the estimation of reflectivity $\hat{\mathbf{x}}$ is given by

$$\hat{\mathbf{x}} = \mathbf{F}\mathbf{y} \tag{20}$$

where $\mathbf{F}$ is an LMMSE filter matching the proposed model

$$\mathbf{F} = \mathbf{R}_{\mathbf{xy}} \mathbf{R}_{\mathbf{y}}^{-\mathbf{1}}. \tag{21}$$

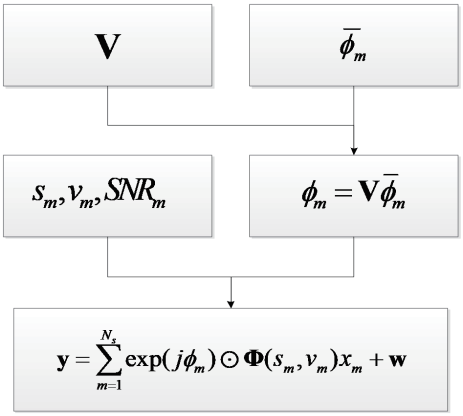

Figure 4. Data simulation flowchart of multi-baseline InSAR.

Table 2. Two groups of scatterers' parameters.

scatterer	Group 1			Group 2		
series	s	v	SNR	s	v	SNR
1	−30m	0mm/yr	10dB	−15m	−1.5mm/yr	8dB
2	10m	0mm/yr	10dB	15m	1.5mm/yr	12dB

With the zero-mean white Gaussian assumption and variance σ_x^2 for the true reflectivity $\mathbf{x}$, the cross-correlation matrix $\mathbf{R_{xy}}$ and autocorrelation matrix $\mathbf{R_y}$ in Eq. (21) are calculated using Eqs. (15) and (16)

$$\mathbf{R_{xy}} = \sigma_x^2 \mu_a \mu_\tau \mu_d \mathbf{\Phi}^{\mathrm{H}} \tag{22}$$

$$\mathbf{R_y} = \sigma_x^2 \mathbf{R_c} \odot (\mathbf{\Phi}\mathbf{\Phi}^{\mathrm{H}}) + \sigma_{\mathrm{w}}^2 \mathbf{I} \tag{23}$$

where σ_θ^2 in μ_a and $\mathbf{R_c}$ is set to the maximum residual phase error according to the accuracy of phase compensation which is not more than 1 empirically, σ_x^2 over σ_{w}^2 is proportional to SNR, ρ_s and ρ_v are less than their respective Rayleigh resolutions, and the other parameters are obtained from the aforementioned equations according to system parameters.

5. Experiments

In this section, simulations on simple pixels and complex scene as well as real data experiment are carried out to validate the practicality of the proposed statistical D-TomoSAR model. The LMMSE estimator is employed for all the compared models, where the LMMSE results of deterministic model and the extended D-TomoSAR model from [11] are compared with the LMMSE results of the proposed model.

Table 3. D-TomoSAR System parameters.

satellite height	off-nadir angle ξ	wavelength λ	number of images
520km	23°	0.03125m	27
temporal interval	temporal span	Spatial baselines	
		regular case	irregular case
32 days	$\frac{7}{3}$ years	equal intervals and baseline span is 300m	uniform distributed in [-150m, 150m]

5.1. Simple pixels

First of all, two groups of simulated stacking data are generated corresponding to two kinds of layover targets, whose parameters are listed in Tab. 2. Each kind of targets is observed under the condition of repeated passes in cases of regular spatial baselines, and irregular baselines with their irregularity following a uniform distribution. The parameters are set close to the TerraSAR-X satellite [8]. All D-TomoSAR system parameters are listed in Tab. 3. The signal-noise-ratio (SNR) is defined as

$$SNR = 10\lg(|x|^2/\sigma_{\mathrm{w}}^2), \tag{24}$$

where $|x|^2$ is the intensity of the scatterers.

The LMMSE estimator is applied to the simulated data and the results are shown in Figs. 5 and 6. In the first group of layover targets, two scatterers with no deformations are set with $\sigma_\theta^2 = 0.16$, elevation interval $\Delta s = 40$m which corresponds to 1.3595 times the elevation Rayleigh resolution, and SNR of two scatterers being $SNR_1 = SNR_2 = 10$dB. As shown in Fig. 5, the elevation-velocity spectrums of two close scatterers are separated and estimated by LMMSE under the extended model from [11] and the proposed model, which demonstrates the effect of umcompensated phase. In the second group of layover targets, two closer scatterers are set with $\sigma_\theta^2 = 0.09$, $\Delta s = 30$m and $\Delta v = 3$mm/yr, which correspond to 1.0196 times the elevation Rayleigh resolution and 0.5973 times the deformation velocity Rayleigh resolution, respectively, $SNR_1 = 8$dB and $SNR_2 = 12$dB. It is observed from Fig. 6 that the LMMSE results of the proposed model are more robust than those of other two models, which demonstrate the effectiveness of the proposed spatial and temporal decorrelation effects. As expected by comparing two groups of figures and both cases of regular and irregular baseline, the sidelobe for the irregular case is higher than that of the regular one and the stronger residual phase noise results in a higher sidelobe level.

5.2. Complex scene

Next, we validate the effectiveness of statistical D-TomoSAR model via 45 SAR images generated by TerraSAR-X system parameters observed on an island digital elevation

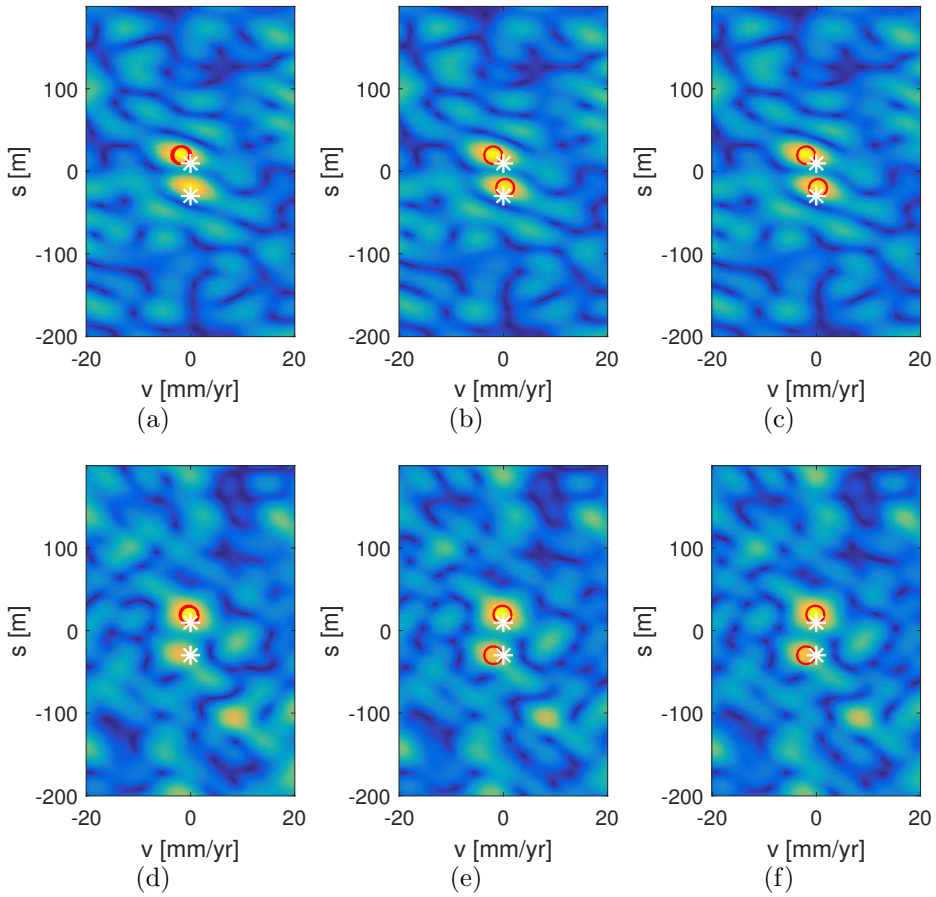

Figure 5. The estimated elevation-velocity spectrums of Group 1, where the red circles represent the estimated positions by maximal detection, while the white asterisks represent the true positions. The results of LMMSE under the condition of regular sampling: (a) deterministic model; (b) the extended model; (c) the proposed model. The results of LMMSE under the condition of irregular sampling: (d) deterministic model; (e) the extended model; (f) the proposed model.

model (DEM). The DEM is shown in Fig. 7 (a), and the whole scene has a size of 2.25Km × 2.25Km. The 45 SAR images are observed without temporal difference. The spatial resolution along azimuth-range direction is 3.30m × 2.04m. The multi-baselines are regularly distributed with spatial interval 12m and a total span 528m. Fig. 7 (b) shows one of the 45 SAR images. In order to facilitate the quantitative evaluation, 99 ground control points (GCPs) are placed evenly and shown in bright dots in Fig. 7 (b).

After preprocessing in Fig. 1, we applied the LMMSE estimator to the three mentioned models. Then, the normalized elevation spectrum is obtained and the possible elevation positions are found from the spectrum peaks. After the order of the model is selected by the BIC criterion [29], the elevation is determined by the position of strong peaks. Finally, the height profile of the whole image is obtained by elevation times the sine of incidence angle.

Fig. 8 shows the height profiles estimated by the LMMSE estimator using the three models in the azimuth-range plane. It is worth noting that when two scatterers

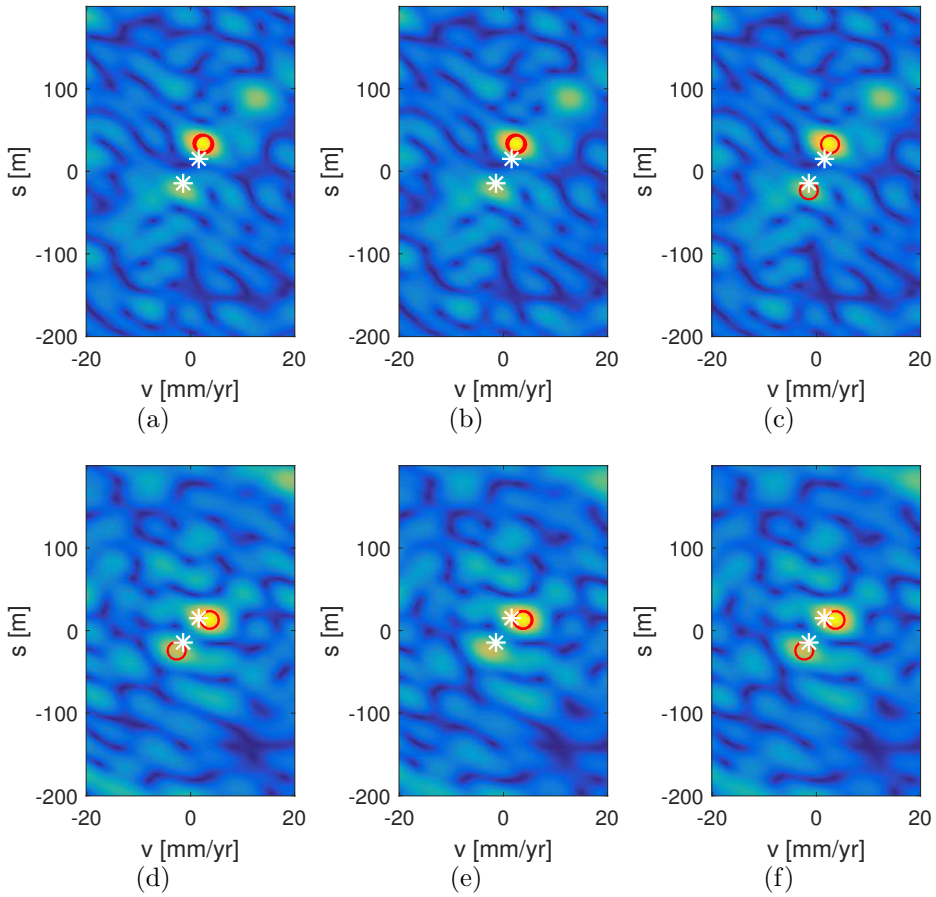

Figure 6. The estimated elevation-velocity spectrums of Group 2, where the red circles represent the estimated positions by maximal detection, while the white asterisks represent the true positions. The results of LMMSE under the condition of regular sampling: (a) deterministic model; (b) the extended model; (c) the proposed model. The results of LMMSE under the condition of irregular sampling: (d) deterministic model; (e) the extended model; (f) the proposed model.

are overlaid in one pixel only the point cloud of the stronger scatterer is shown. By comparing the reconstructed results of Fig. 8 with truth height of Fig. 7 (a), it is observed that all the three models are effective in reconstructing the height profile. Subsequently, the relative accuracy is evaluated from the results of 99 GCPs, and the number of effectively detected pixels in the whole SAR image is counted. The results are listed in Tab. 4. It can be seen that the LMMSE under the proposed model is the most accurate. Moreover, the number of effectively detected pixels under the statistical model is the largest, which shows that the best reconstruction result has been achived by our model for extended scatterers.

5.3. Real data

Finally, 20 passes real data acquired by the sensors of TerraSAR-X/Tandem-X, over Terminal 3-E (T3-E) of the Beijing Capital International Airport, between 2012 and

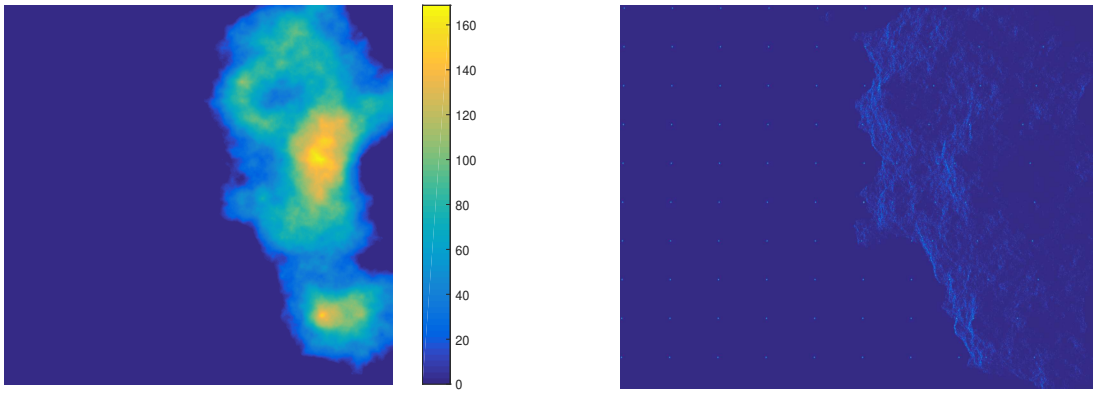

(a) (b)

Figure 7. A complex scene. (a) The truth DEM; (b) one of the 45 SAR images.

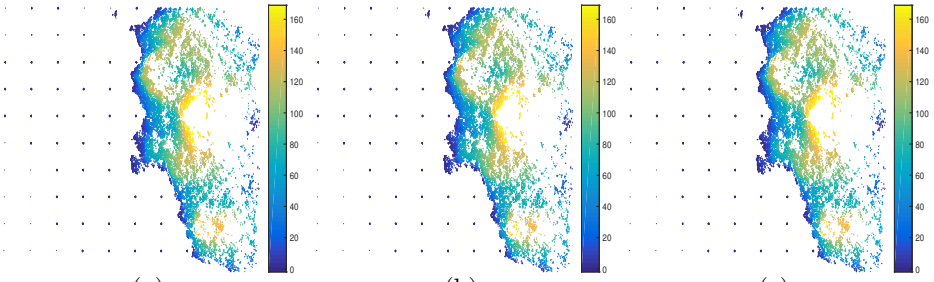

(a) (b) (c)

Figure 8. LMMSE results of different model: (a) Deterministic model; (b) the extended model; (c) the proposed model.

Table 4. Relative accuracy of 99 GCPs and comparison of the number of detected pixels.

Type of model	LMMSE based on Bic detector	
	relative accuracy	number of detected pixels
deterministic model	0.7743m	32891
extended model	0.5415m	32939
proposed model	0.5263m	32952

2014, are utilized for demonstration. Detailed information about the real data can be found in [31]. One of the SAR intensity images is shown in Fig. 9 (a), where one arbitrary overlayed pixel is chosen for validation. The selected pixel marked by the red point is overlaid by the ground scatterer and eave scatterer. Fig. 9 (b) shows the acquisition geometry of the selected pixel. The eave height relative to the ground is about 27.7710m [31]. The LMMSE elevation-velocity spectrums of three models are shown in Fig. 10. Table 5 lists the LMMSE results. It is observed that the result of proposed model is the most accurate in terms of not only the height but also the deformation velocity.

Table 5. The estimated height and deformation velocity of two scatterers.

Type of model	scatterer 1 (eave)	scatterer 2 (ground)
deterministic model	(56.7791m,-17.5mm/yr)	(-4.2903m,19.9mm/yr)
extended model	(27.8677m,-1.5mm/yr)	(54.9238m,-17.5mm/yr)
proposed model	(27.8677m,-1.5mm/yr)	(0.0387m,2.7mm/yr)

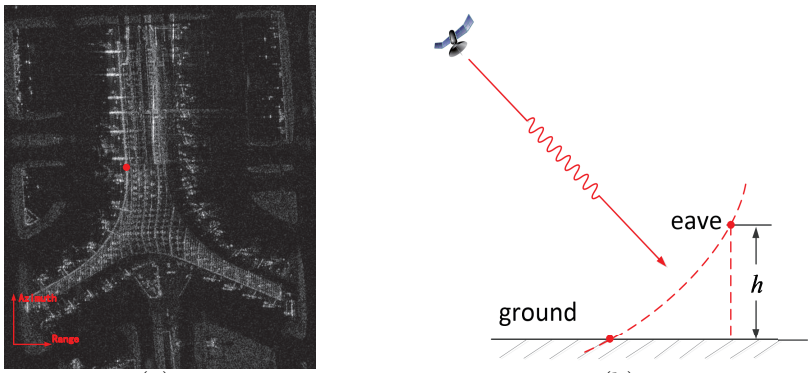

Figure 9. T3-E of Beijing Capital International Airport. (a) TerraSAR-X intensity image; (b) acquisition geometry of the red pixel.

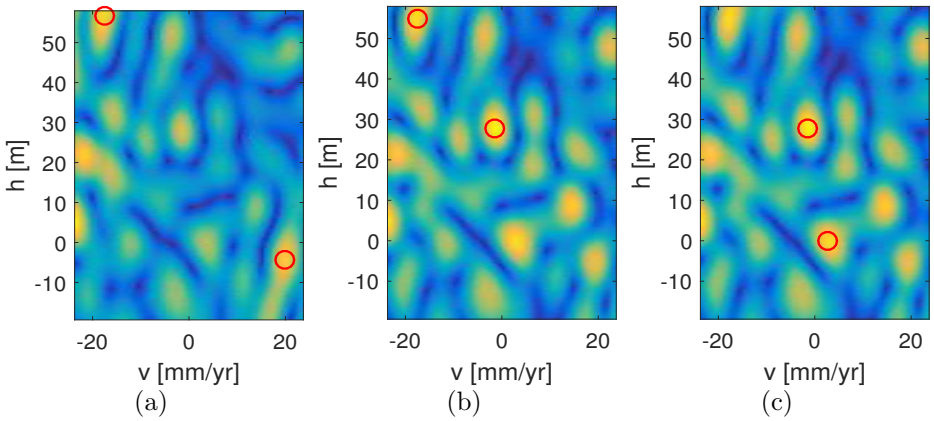

Figure 10. The LMMSE elevation-velocity spectrums of three models, where the red circles represent the estimated positions by maximal detection: (a) Deterministic model; (b) the extended model; (c) the proposed model.

6. Conclusion

Phase miscalibration resulting from the scattering changes from temporal and spatial decorrelation effects as well as the residual effects after preprocessing is a primary factor affecting the accuracy of elevation and deformation velocity in D-TomoSAR. In this paper, the correlation of targets has been analysed theoretically according to the 4-D imaging mechanism, and then a statistical model to account for phase miscalibration has been proposed. Furthermore, a simulator for D-TomoSAR data generation is designed

based on the proposed model, and an LMMSE estimator is derived to reconstruct the scattering position in the elevation-velocity plane. Using the simulated stacking data with realistic effects and SAR images observed by the TerraSAR-X/Tandem-X system, the effectiveness of the proposed model was demonstrated by LMMSE estimation results. In the future, we will consider using the statistical model for performance prediction and system/algorithm design.

Acknowledgement

This work is funded by the National Natural Science Foundation of China (no. 61471020) and Science and Technology Research Project of Education Department of Hubei (no. Q20172505).

References

[1] Fornaro G, Lombardini F, Pauciullo A, Reale D and Viviani F 2014 Tomographic Processing of Interferometric SAR Data: Developments, applications, and future research perspectives *IEEE Signal Processing Magazine* **31** 41–50

[2] Zhu X X and Bamler R 2014 Superresolving SAR Tomography for Multidimensional Imaging of Urban Areas: Compressive sensing-based TomoSAR inversion *IEEE Signal Processing Magazine* **31** 51–58

[3] Fornaro G and Pascazio V 2014 Sar interferometry and tomography: Theory and applications *Academic Press Library in Signal Processing* vol 2 (Elsevier) pp 1043–1117

[4] Reigber A and Moreira A 2000 First demonstration of airborne SAR tomography using multibaseline L-band data *IEEE Transactions on Geoscience and Remote Sensing* **38** 2142–2152

[5] Budillon A and Schirinzi G 2016 GLRT based on support estimation for multiple scatterers detection in SAR tomography *IEEE Journal of Selected Topics in Applied Earth Observations and Remote Sensing* **9** 1086–1094

[6] Fornaro G, Lombardini F and Serafino F 2005 Three-dimensional multipass SAR focusing: experiments with long-term spaceborne data *IEEE Transactions on Geoscience and Remote Sensing* **43** 702–714

[7] Fornaro G, Serafino F and Soldovieri F 2003 Three-dimensional focusing with multipass SAR data *IEEE Transactions on Geoscience and Remote Sensing* **41** 507–517

[8] Zhu X X and Bamler R 2010 Very High Resolution Spaceborne SAR Tomography in Urban Environment *IEEE Transactions on Geoscience and Remote Sensing* **48** 4296–4308

[9] Lombardini F 2005 Differential tomography: a new framework for SAR interferometry *IEEE Transactions on Geoscience and Remote Sensing* **43** 37–44

[10] Budillon A, Johnsy A C and Schirinzi G 2017Extension of a Fast GLRT Algorithm to 5D SAR Tomography of Urban Areas *Remote Sensing* **9** 844

[11] Fornaro G and Pauciullo A 2009 LMMSE 3-D SAR Focusing *IEEE Transactions on Geoscience and Remote Sensing* **47** 214–223

[12] Rodriguez E and Martin J M 1992 Theory and design of interferometric synthetic aperture radars *IEE Proceedings F Radar and Signal Processing* **139** 147–159

[13] Ferretti A, Colesanti C, Perissin D, Prati C and Rocca F 2003 Evaluating the effect of the observation time on the distribution of sar permanent scatterers *FRINGE 2003 Workshop*

[14] Berardino P, Fornaro G, Lanari R and Sansosti E 2002 A new algorithm for surface deformation monitoring based on small baseline differential SAR interferograms *IEEE Transactions on Geoscience and Remote Sensing* **40** 2375–2383

[15] Lanari R, Casu F, Manzo M, Zeni G, Berardino P, Manunta M and Pepe A 2007 An Overview of the Small BAseline Subset Algorithm: a DInSAR Technique for Surface Deformation Analysis *Pure Applied Geophysics* **164** 637–661

[16] Gini F and Lombardini F 2005 Multibaseline cross-track SAR interferometry: a signal processing perspective *IEEE Aerospace and Electronic Systems Magazine* **20** 71–93

[17] Rocca F 2007 Modeling Interferogram Stacks *IEEE Transactions on Geoscience and Remote Sensing* **45** 3289–3299

[18] Pauciullo A, Maio A D, Perna S, Reale D and Fornaro G 2014 Detection of Partially Coherent Scatterers in Multidimensional SAR Tomography: A Theoretical Study *IEEE Transactions on Geoscience and Remote Sensing* **52** 7534–7548 0196-2892

[19] Fornaro G and Serafino F 2006 Imaging of single and double scatterers in urban areas via SAR tomography *IEEE Transactions on Geoscience and Remote Sensing* **44** 3497–3505

[20] Ferretti A, Prati C and Rocca F 2001 Permanent scatterers in SAR interferometry *IEEE Transactions on Geoscience and Remote Sensing* **39** 8–20

[21] Lombardini F and Pardini M 2012 Superresolution Differential Tomography: Experiments on Identification of Multiple Scatterers in Spaceborne SAR Data *IEEE Transactions on Geoscience and Remote Sensing* **50** 1117–1129

[22] Zhu X X and Bamler R 2011 Let's Do the Time Warp: Multicomponent Nonlinear Motion Estimation in Differential SAR Tomography *IEEE Geoscience and Remote Sensing Letters* **8** 735–739

[23] Fornaro G, Reale D and Serafino F 2009 Four-Dimensional SAR Imaging for Height Estimation and Monitoring of Single and Double Scatterers *IEEE Transactions on Geoscience and Remote Sensing* **47** 224–237

[24] Agram P S and Simons M 2015 A noise model for InSAR time series *Journal of Geophysical Research: Solid Earth* **120** 2752–2771

[25] Pauciullo A, De Maio A, Perna S, Reale D and Fornaro G 2013 Detection of partially coherent scatterers in multidimensional sar tomography: a theoretical study *SAR Image Analysis, Modeling, and Techniques XIII* vol 8891 (International Society for Optics and Photonics) p 889106

[26] Guarnieri A M and Tebaldini S 2008 On the Exploitation of Target Statistics for SAR Interferometry Applications *IEEE Transactions on Geoscience and Remote Sensing* **46** 3436–3443

[27] Perissin D and Wang T 2012 Repeat-Pass SAR Interferometry With Partially Coherent Targets *IEEE Transactions on Geoscience and Remote Sensing* **50** 271–280

[28] KAY S M 1998 *Fundamentals of Statistical Signal Processing* (New Jersey: Prentice Hall)

[29] Burnham K P and Anderson D R 2004 Multimodel inference: understanding AIC and BIC in model selection *Sociological methods & research* **33** 261–304

[30] Wang C, Wang G, Zhu Z and Ke C 2008 Structure Design of Beijing Capital International Airport Terminal 3 *Building Structure* **38** 16–24

[31] Yang B, Xu H, Liu W, You Y and Xie X 2018 Realistic Lower Bound on Elevation Estimation for Tomographic SAR *IEEE Journal of Selected Topics in Applied Earth Observations and Remote Sensing* 1–11

Appendix A. Derivation of the Correlation Function

Based on Eqs. (4) and (5) and the definition of correlation function, the correlation function of 4-D focusing can be derived:

$$
\begin{aligned}
&E\left[x_{k_1}\left(s_{m_1},v_{n_1}\right)x_{k_2}(s_{m_2},v_{n_2})^*\right]\\
&=E\left[\exp(j\theta_{k_1}-j\theta_{k_2})\right]\cdot\\
&\quad E\left\{\begin{array}{l}\int_{s_{m_1}-\frac{\rho_s}{2}}^{s_{m_1}+\frac{\rho_s}{2}}\int_{v_{n_1}-\frac{\rho_v}{2}}^{v_{n_1}+\frac{\rho_v}{2}}\gamma\left(s_1,v_1\right)e^{j2\pi\xi_{k_1}(s_1-s_{m_1})-j2\pi\eta_{k_1}(v_1-v_{n_1})}ds_1dv_1\cdot\\ \int_{s_{m_2}-\frac{\rho_s}{2}}^{s_{m_2}+\frac{\rho_s}{2}}\int_{v_{n_2}-\frac{\rho_v}{2}}^{v_{n_2}+\frac{\rho_v}{2}}\gamma(s_2,v_2)^*e^{j2\pi\eta_{k_2}(v_2-v_{n_2})-j2\pi\xi_{k_2}(s_2-s_{m_2})}ds_2dv_2\end{array}\right\}\\
&=\frac{\sigma_x^2}{\rho_s\rho_v}(\mu_a^2)^{1-\hat{\delta}(k_1-k_2)}\\
&\qquad\cdot\left[\begin{array}{l}\int_{-\frac{\rho_s}{2}}^{\frac{\rho_s}{2}}\int_{-\frac{\rho_s}{2}}^{\frac{\rho_s}{2}}\delta(s_1+s_{m_1}-s_2-s_{m_2})e^{j2\pi\xi_{k_1}s_1-j2\pi\xi_{k_2}s_2}ds_1ds_2\cdot\\ \int_{-\frac{\rho_v}{2}}^{\frac{\rho_v}{2}}\int_{-\frac{\rho_v}{2}}^{\frac{\rho_v}{2}}\delta(v_1+v_{n_1}-v_2-v_{n_2})e^{j2\pi\eta_{k_2}v_2-j2\pi\eta_{k_1}v_1}dv_1dv_2\end{array}\right]\\
&=\frac{\sigma_x^2}{\rho_s\rho_v}(\mu_a^2)^{1-\hat{\delta}(k_1-k_2)}\hat{\delta}(s_{m_1}-s_{m_2})\hat{\delta}(v_{n_1}-v_{n_2})\cdot\int_{-\frac{\rho_s}{2}}^{\frac{\rho_s}{2}}e^{\frac{j4\pi s(b_{\perp k_1}-b_{\perp k_2})}{\lambda r}}ds\\
&\qquad\cdot\int_{-\frac{\rho_v}{2}}^{\frac{\rho_v}{2}}e^{\frac{j4\pi v(t_{k_2}-t_{k_1})}{\lambda}}dv\\
&=\sigma_x^2\mu_a^{2-2\hat{\delta}(k_1-k_2)}\hat{\delta}(s_{m_1}-s_{m_2})\hat{\delta}(v_{n_1}-v_{n_2})sinc(\frac{2\rho_s\triangle\mathbf{b}_{k_1k_2}}{\lambda r})sinc(\frac{2\rho_v\triangle\mathbf{t}_{k_1k_2}}{\lambda})
\end{aligned}
$$

It is worth noting that once the interval division of the elevation direction is determined, the elevation s_{m_i} and deformation v_{n_i} of the m_in_i-th patch are determined for $m_i = 1,2,\cdots,M$, $n_i = 1,2,\cdots,N$ $(i=1,2)$, and thus

$$
\begin{aligned}
&\delta(s_1+s_{m_1},s_2+s_{m_2})=\delta(s_1,s_2)\hat{\delta}(s_{m_1},s_{m_2})\\
&\delta(v_1+v_{n_1},v_2+v_{n_2})=\delta(v_1,v_2)\hat{\delta}(v_{n_1},v_{n_2})
\end{aligned}
$$

for $s_i\in(-\frac{\rho_s}{2},\frac{\rho_s}{2})$, $v_i\in(-\frac{\rho_v}{2},\frac{\rho_v}{2})$ $(i=1,2)$. This is why $\hat{\delta}(s_{m_1},s_{m_2})$ and $\hat{\delta}(v_{n_1},v_{n_2})$ appear in the third equation above.